# Coastal wind retrievals from corrected QuikSCAT Normalized Radar Cross Sections

Giuseppe Grieco [a,*], Marcos Portabella [b], Ad Stoffelen [c], Anton Verhoef [c], Jur Vogelzang [c], Andrea Zanchetta [d], Stefano Zecchetto [e,f]

[a] *Istituto di Scienze Marine - Consiglio Nazionale delle Ricerche (ISMAR-CNR), Calata Porta di Massa, Napoli, 80133, Italy*
[b] *Barcelona Expert Center (BEC), Institut de Ciencies del Mar (ICM-CSIC), Paseig Maritim de la Barceloneta, 37, Barcelona, 08003, Spain*
[c] *Koninklijk Nederlands Meteorologisch Instituut (KNMI), Utrechtseweg, 297, De Bilt, 3731GA, Netherlands*
[d] *Department of Music - Hong Kong Baptist University, Sing Tao Building, Kowloon Tong, Hong Kong Special Administrative Region of China*
[e] *Istituto di Scienze Polari - Consiglio Nazionale delle Ricerche (ISP-CNR), Corso Stati Uniti, 4, Padova, 35127, Italy*
[f] *Faculty of Intelligent Systems Engineering and Data Science - Persian Gulf University, Bushehr, 7516913817, Iran*

## ARTICLE INFO

## ABSTRACT

A new correction scheme named "noise regularization", aiming at mitigating land contamination in SeaWinds scatterometer coastal Normalized Radar Cross Sections ($\sigma_0$s) is presented. The scheme is based on an analytical Cumulative Distribution Function (CDF) matching technique. Its efficacy is demonstrated in a semi-enclosed basin of the Mediterranean Sea, both in the $\sigma_0$ and wind field domains. Wind biases along the coasts disappear and the sampling improves by a factor of 3 within the first 10 km from the coastline. This figure is likely underestimated because of a non-optimal tuning of the a-posteriori quality control tests in coastal areas.

Finally, wind retrievals are validated against those from a collocated Synthetic Aperture Radar (SAR) image acquired by the Envisat Advanced SAR (ASAR) offshore Norway. The agreement is very good in both speed and direction, and opens new perspectives on the use of SAR as a validation tool of coastal winds.

## 1. Introduction

According to the United Nations (UN), about 40% of the world's human population lives along the coasts. Their lives are heavily affected by coastal atmospheric and oceanographic phenomena, such as land and sea breezes, katabatic winds, coastal marine currents, etc. Even if many of these phenomena have a theoretical basic explanation, the lack of high-spatial-resolution accurate measurements of winds and currents hampers the full comprehension of air–sea fluxes, the interaction with local orography, the impacts on local biology, and, more in general, how coastal areas mediate between inland and open ocean. In all these phenomena, wind plays a key role, especially if one thinks to coastal upwelling, dispersion of pollutants, erosion, etc.; but it also plays a non-negligible role in civil matters, such as power generation by off-shore plants, search and rescue operations, extreme events risk mitigation, touristic activities, etc.

In Bourassa et al. (2019), the authors highlight the observational gaps and needs to properly sample coastal winds, both in space and time, for a wide range of scientific challenges, such as a better comprehension of coastal processes and ecosystems. Today, scatterometer-derived winds represent the gold standard due to their unmatched

accuracy, better than 1 ms$^{-1}$ in speed and $\pm20°$ in direction (Vogelzang and Stoffelen, 2022b). In addition, uninterrupted multidecadal records of ocean winds by satellite scatterometer missions represents an invaluable asset for climate change monitoring. Unfortunately, coastal scatterometer measurements may be contaminated by land up to approximately 30 km from the coastline. In fact, the typical largest linear dimension of a satellite scatterometer footprint such as the C-band, fan-beam Advanced Scatterometer (ASCAT) and the Ku-band, dual pencil-beam Quick Scatterometer (QuikSCAT) is on the order of 20–30 km (Anderson et al., 2012; Spencer et al., 2000). Note that, thanks to range filtering, scatterometer footprints are resolved into smaller asymmetric footprints, which in the case of QuikSCAT are called slices (Spencer et al., 2000). In addition, note that the footprint size refers to the Spatial Response Function (SRF) −3 dB contour; therefore, residual land contamination can be present up to 50–60 km from the coast (Owen and Long, 2009). It turns out that coastal wind retrievals may be biased, and quality control flags are often within about 30 km to the coastline.

In the last two decades, several strategies have been implemented to mitigate land contamination. In Owen and Long (2009), the authors

---

defined the so-called Land Contribution Ratio (LCR) index, which is a weighted average of a land/sea mask (LSM) database by means of the SRF values. Of course, the accuracy of LCR depends on the spatial resolution of both LSM and SRF. LCR values were then used to filter out excessively contaminated measurements. LCR thresholds were dynamically set according to the context, but were generally lower than 2%, due to the high contrast between land and sea Normalized Radar Cross Sections ($\sigma_0$s). In fact, land $\sigma_0$s may be up to more than 10 dB larger than sea $\sigma_0$s. LCR has also been used in other studies. Recently, Soisuvarn et al. (2023) have applied the LCR method to ASCAT acquisitions with a double purpose: (a) to estimate the area of the footprint contaminated by land; (b) to estimate a "coarse" land contribution to $\sigma_0$ ($\sigma_0^L$) in combination with the weighted average algorithm (Early and Long, 2001). Then, an iterative algorithm is implemented to calculate a finer estimate of $\sigma_0^L$. Finally, this estimate is subtracted from the land-contaminated $\sigma_0$ to isolate the sea component. In Fore et al. (2022), the authors subtract $\sigma_0^L$ from the contaminated QuikSCAT measurements in a similar fashion. Differences are mainly related to the methodology used to estimate $\sigma_0^L$. In the mentioned study, $\sigma_0^L$s are accumulated over the entire QuikSCAT mission (1999–2009) on a monthly basis to calculate LCR Estimated $\sigma_0^L$s. According to the authors, this methodology is a combination of the LCR and the Empirical Land Mask (ELM) (Vanhoff et al., 2013) methods. In the ELM method, LSM is empirically derived by setting a threshold on the specific $\sigma_0$ variability. Areas with specific $\sigma_0$ variability higher than a given threshold are identified as marine areas. Finally, in Vogelzang and Stoffelen (2022a), the authors show how to estimate ASCAT $\sigma_0^L$s using a Least Square method, supposing that $\sigma_0$ dependency on LCR is linear and that $\sigma_0$ variability is locally negligible both on land and sea.

In all these applications, coastal sampling dramatically improves and accuracy degradation is limited. Even if all of them prove to be effective, the scatterometer community encourages the development of new original correction methodologies to discover the limits and advantages of each technique.

In this paper, a new $\sigma_0$ correction scheme called "noise regularization" is presented, with application to QuikSCAT measurements.

The paper is structured as follows: Section 2 describes the dataset used. Section 3 describes the correction methodology in detail (3.1) and summarizes the consolidated inversion methodology used to retrieve the winds from QuikSCAT measurements (3.2). Section 3.3 briefly describes the scheme used to retrieve winds from Envisat Advanced Synthetic Aperture Radar (ASAR) images. Section 4 shows the results of an application and comparison of QuikSCAT-derived winds with the collocated SAR-derived winds estimated from an ASAR image. Finally, Section 5 reports the discussion and conclusions, together with some plans for future developments.

## 2. Dataset

In this section, the dataset of QuikSCAT Full Resolution (FR) files used for the application of noise regularization is described, together with the Quality Control (QC) applied. Note that Full Resolution is used as synonym of Level 1B in this context. Furthermore, the ASAR images used for validation are also described in a separate subsection.

### 2.1. QuikSCAT full resolution (FR) files

The QuikSCAT mission was launched in 1999 on a sun-synchronous polar orbit. Its unique payload consisted of the SeaWinds scatterometer. Its ascending Local Equatorial Crossing Time (LECT) is 6 A.M. SeaWinds is a conically scanning Ku-band (13.5 GHz) pencil-beam scatterometer consisting of two antennas. The inner (outer) one sends and receives a horizontally (vertically)-polarized signal impinging on the Earth surface with an incidence angle of about 46° (54°) (Spencer et al., 2000).

Acquisitions are stored in time-order fashion. Antenna pulses' echoes are organized in frames with a rate of 100 pulses per frame.

**Table 1**

Meaning of the `sigma0_qual_flag` bits used for QC when the bit is set to 0 (absence of condition), as extracted from QuikSCAT user's manual (Lungu and Callahan, 2006). Bits from 10 to 16 are always set to 0 and are not reported for the sake of brevity.

| bit | Meaning |
| --- | --- |
| 0 | Measurement is usable |
| 1 | SNR level is acceptable |
| 2 | $\sigma_0 \geq 0$ |
| 3 | $\sigma_0$ is in acceptable range |
| 4 | Scatterometer pulse quality is acceptable |
| 5 | $\sigma_0$ cell location algorithm converges |
| 6 | Frequency shift is within the range of the $x$ factor table |
| 7 | Spacecraft temperature is within calibration coefficient range |
| 8 | An applicable attitude record was found for this $\sigma_0$ |
| 9 | Interpolated ephemeris data are acceptable for this $\sigma_0$ |

Pulses' echoes are also called "eggs", recalling the typical elliptical shape of SeaWinds footprints. Thanks to range filtering, each egg is resolved into eight different slices. QuikSCAT FR files provide both egg and slice measurements together with some ancillary information. Egg (slice) measurements and related fields are organized in 2D (3D) time-ordered arrays, whose dimensions are (`frame`, `pulse`) ((`frame`, `pulse`, `slice`)). Each FR file contains the acquisitions of an entire orbit (revolution). The total number of frames per orbit is variable, with typical values of 11,000+.

Noise regularization has been applied to a set of fifteen QuikSCAT FR version 2 files, fourteen of which cover the entire day 10th of April 2007. The last one is dated 24th of November 2008 and is used in this paper for validation purposes. In fact, it is collocated in space and time with the ASAR image described in Section 2.2. They are identified by revolution numbers (IDs) ranging from 40651 to 40664 and 49132, and can be withdrawn from the Physical Oceanography Distributed Active Archive Center (PO.DAAC) catalogue for free, upon registration (SeaPAC, 2006). The full list of QuikSCAT FR files is reported in Table A.5 for the sake of repeatability.

QuikSCAT FR files are provided with some quality flags, namely `frame_err_status`, `frame_qual_flag`, `sigma0_qual_flag` and `slice_qual_flag` among others. The first two flags refer to the entire frame (set of 100 pulses), while the third one reports on the quality of each pulse; the fourth reports on the quality of each slice of the egg. It is required that bit 4 of `frame_qual_status` is set to 0, and bit 0 of `frame_err_status` is set to 0. The former ensures that telemetry data are good in the entire QuikSCAT frame, while the latter states that telemetry does not report any errors. `sigma0_qual_flag` consists of 16 bits, the first 10 of which are informative, while the remaining are always set to 0. For this study, bits 0 and 3 to 9 are required to be 0 (absence of condition). The meaning of each bit is detailed in Table 1 for the sake of clarity, as from the QuikSCAT user's manual (Lungu and Callahan, 2006).

The following statistics refer to the subset dated 10th of April 2007. For this subset, 0.66% of the eggs are discarded, of which 0.65% due to `sigma0_qual_flag`. Once a given egg passes this QC, the `slice_qual_flag` is applied in the wind-retrieval procedure. `slice_qual_flag` consists of 32 bits, four per each of the eight slices. In particular, it is required that bits 0, 2 and 3 of each slice are set to 0. The meaning of each slice bit is reported in Table 2.

A total of 81,172,442 QCed slices are processed by the pencil-beam Wind Processor (PenWP) (Verhoef et al., 2022), which represent 94.8% of the slices over sea. Of these, 2.96% are good quality slices with negative $\sigma_0$.

### 2.2. ASAR files

In this work, an Envisat ASAR Wide Swath Medium Resolution (WSM) image at VV polarization and 75 m pixel size has been used. It has been downloaded for free from the ESA User Service Portal,

**Table 2**
Meaning of the 4-bit slice set of `slice_qual_flag` used for QC when the bit is set to 0 (absence of condition), as extracted from QuikSCAT user's manual (Lungu and Callahan, 2006). SNR stands for Signal to Noise Ratio.

| bit | Meaning |
|-----|---------|
| 0 | Gain exceeds peak gain threshold |
| 1 | $\sigma_0 \geq 0$ |
| 2 | SNR level is acceptable |
| 3 | Slice center located |

upon registration, at the following link https://esar-ds.eo.esa.int/oads/access/collection/ASA_WSM_1P. The name of this image is listed at the end of Table A.6. A wind field at 900 m pixel has been retrieved using a methodology based on the Convolutional Neural Network (CNN) (Zanchetta and Zecchetto, 2021) described in Section 3.3, and used to validate QuikSCAT-derived coastal winds. The CNN scheme is trained with the ASAR WSM images listed in the first 27 rows of Table A.6.

## 3. Methodology

The empirical methodology used to correct land-contaminated slice $\sigma_0$s is described in Section 3.1. In addition, the inversion methodology of QuikSCAT acquisitions implemented in PenWP is briefly summarized in Section 3.2.

### 3.1. Noise regularization

Noise regularization is based on the Cumulative Distribution Function (CDF) matching technique and on the following linear model for land-contaminated $\sigma_0$s :

$$\sigma_{0,f} = (1-f)\bar{\sigma}_{0,S} + f\bar{\sigma}_{0,L} + \underbrace{(1-f)\epsilon_S + f\epsilon_L}_{\epsilon} \tag{1}$$

where $f$ stands for LCR, $S$ for sea, $\epsilon$ represents the variability and $\bar{\phantom{.}}$ the expectation operator. The dependency of $\sigma_0$ on $f$ is indicated with the subscript $f$. Note that the symbol $S$ ($L$) stands for $f = 0$ ($f = 1$). This writing emphasizes the fact that $\epsilon$ arises due to random $\sigma_0$ variability and to every kind of noise sources on sea ($\epsilon_S$) and land ($\epsilon_L$), respectively). This means that if one estimates $\bar{\sigma}_{0,L}$ and then subtracts it from $\sigma_{0,f}$, the resulting estimate of $\sigma_{0,S}$ will be affected by two deviations, the land component of which can be 10 to 100 times larger in magnitude than the sea component. For SeaWinds, this can lead to unrealistic negative estimates of $\sigma_{0,S}$s (Grieco et al., 2022c).

With two unknowns ($\bar{\sigma}_{0,S}$, $\bar{\sigma}_{0,L}$) and one measurement ($\sigma_{0,f}$), Eq. (1) is an underdetermined problem. In the proposed method, the CDF of the random variable $\sigma_{0,f}$ is analytically modeled for both sea and contaminated acquisitions; then, a CDF matching is imposed, and $\sigma_{0,S}$ is obtained from Eq. (2):

$$\sigma_{0,S} = F_S^{-1}(F_f(\sigma_{0,f})) \tag{2}$$

where $F_S$ ($F_f$) is the CDF of $\sigma_{0,S}$ ($\sigma_{0,f}$).

In Spencer et al. (2000), the authors derive the variability relationship and the $K_p$ for Seawinds. However, $\sigma_0$ pdf can be reasonably modeled as a normalized $\chi^2$, as demonstrated in Grieco et al. (2022b) and described by Eq. (3)

$$pdf_{\sigma_{0,f}}(\alpha_{\bar{\sigma}_0}, k) = \frac{1}{\alpha_{\bar{\sigma}_0} 2^{\frac{k}{2}} \Gamma(\frac{k}{2})} \left(\frac{\sigma_0}{\alpha_{\bar{\sigma}_0}}\right)^{\frac{k}{2}-1} \exp{-\frac{\sigma_0}{2\alpha_{\bar{\sigma}_0}}} \tag{3}$$

$$F_{\sigma_{0,f}}(\alpha_{\bar{\sigma}_0}, k) = P(\frac{k}{2}, \frac{\sigma_0}{2\alpha_{\bar{\sigma}_0}}) \tag{4}$$

$$\alpha_{\bar{\sigma}_0} = \frac{\bar{\sigma}_0}{k} \tag{5}$$

$$k = \frac{2}{K_p^2} \tag{6}$$

where $k$ stands for degrees of freedom, $\sigma$ (without subscript 0) for standard deviation, $K_p$ is the $\sigma_0$ noise normalized standard deviation and $P(a, x)$ is the regularized incomplete gamma function, defined in Grieco et al. (2022b) as

$$P(a, x) = \frac{1}{\Gamma(a)} \int_0^x t^{a-1} e^{-t} dt \tag{7}$$

The dependency of $pdf_{\sigma_{0,f}}$ and $F_{\sigma_{0,f}}$ on $\alpha_{\bar{\sigma}_0}$ and $k$ has been explicitly indicated for the sake of clarity. Both parameters can be derived from Eqs. (5) and (6), respectively, given that one knows $\bar{\sigma}_0$ and $K_p$.

Note that $k$ is the double of the equivalent number of looks and is inversely proportional to $K_p^2$. In other words, the higher is $K_p$, the lower the equivalent number of looks is.

The CDFs of the contaminated and non contaminated $\sigma_0$s are unambiguously determined by the parameters $\bar{\sigma}_0$ and $K_p$.

In this study, $\bar{\sigma}_{0,f}$ (the expected value of the contaminated $\sigma_0$s) is estimated with a Least Square method, as described in Vogelzang and Stoffelen (2022a). In particular, all the acquisitions dropping in a $5 \times 5$ matrix of Wind Vector Cells (WVCs) surrounding the WVC over which the correction is applied, are used to fit the linear trend of $\bar{\sigma}_{0,f}$ with respect to $f$, for each of the four flavors. Since the WVC spacing is 12.5 km, the matrix covers an area of $62.5 \times 62.5$ km$^2$. In this paper, $f$ is obtained with the following formula:

$$f = \frac{\sum_{ij} S_{ij} LSM_{ij}}{\sum_{ij} S_{ij}} \tag{8}$$

with $LSM_{ij}$ the Land–Sea Mask values at the grid points $(i, j)$ where the Spatial Response Function of the slice ($S_{ij}$) is defined. To speed-up the computation, $S$ is queried from a look-up table (LUT) of pre-computed Spatial Response Functions that are parameterized with respect to the orbit time, latitude and acquisition azimuth angle. This LUT and the ancillary software were kindly provided by the Brigham Young University.

The goodness of the linear fit is evaluated with the mean square error (MSE) of the regression, computed with the following formula:

$$\sigma_e^2 = \frac{n}{n-2}(C_{\sigma_0\sigma_0} - 2aC_{f\sigma_0} + a^2 C_{ff}) \tag{9}$$

with $n$ the number of $(f, \sigma_0)$ pairs in the regression, $C_{\sigma_0\sigma_0}$ ($C_{ff}$) the second central moment of $\sigma_0$ ($f$), $C_{f\sigma_0}$ the covariance of $\sigma_0$ and $f$, and $a$ the slope.

Fig. 1 shows how the fitting procedure works. In Fig. 1(a), the $5 \times 5$ cyan-red matrix represents an extraction of the level 2 WVC grid where the retrievals are performed. Slice centroids are represented with circular markers, whose colors represent the $\sigma_0$ values in logarithmic units (dB), using a gray color map. All the acquisitions dropping in this $5 \times 5$ matrix are used to fit $\bar{\sigma}_{0,f}$, for each of the four "flavors": $\{H - Pol; aft\}$ (HHA), $\{H - Pol; fore\}$ (HHF), $\{V - Pol; aft\}$ (VVA) and $\{V - Pol; fore\}$ (VVF), as shown in Fig. 1(b). On a first instance, $\bar{\sigma}_{0,S}$ is estimated from data, by averaging all the acquisitions of a given flavor in the matrix with LCR lower than 2%. If this set is empty, $\bar{\sigma}_{0,S}$ is set equal to the absolute term of the linear fit of $\bar{\sigma}_{0,f}$. If also this estimate is negative, all the acquisitions in the target WVC are flagged. This occurrence involves only 10 slices over 81,172,442. Finally, Fig. 1(c) shows the scatter plot after noise regularization is applied. Note that the $y$-axis limits are much smaller than in Fig. 1(b). Furthermore, the fluctuations of the corrected values are much reduced and homogeneous. The method is named "noise regularization" since the level of noise does not depend on the degree of land contamination after the correction is applied.

The LCR threshold value of 2% was set in the past for operational purposes, before any coastal correction was developed. Typical land and sea backscatter coefficients were computed; then the distortion of the sea backscatter due to land contamination was evaluated. This
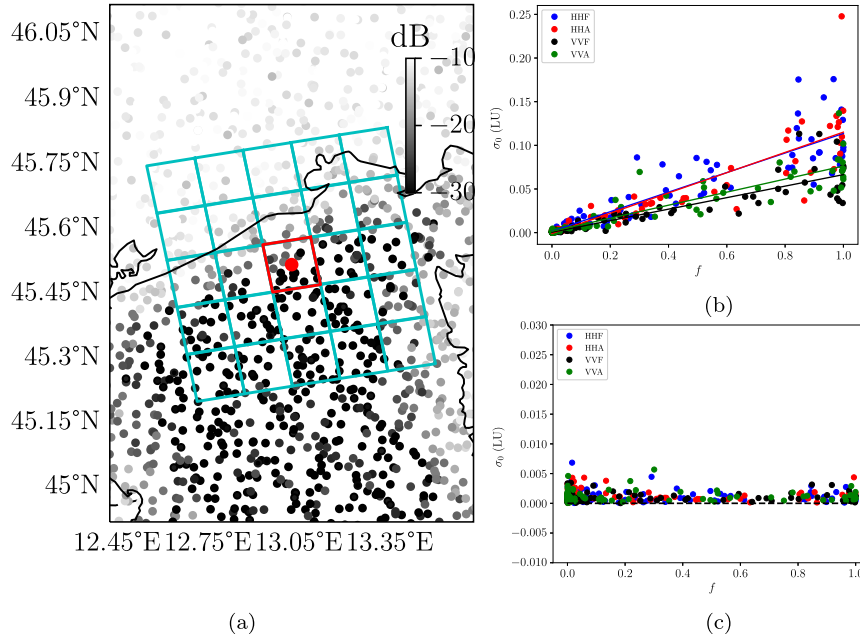
(a)



(b)



(c)

**Fig. 1.** Left: map of $\sigma_0$s in logarithmic units (dB) in a coastal area of the Adriatic, in the Mediterranean Sea. Gray markers represent the slice centroids. Their colors represent the $\sigma_0$ values in logarithmic units (dB). Red-framed box: WVC over which noise regularization is applied. Cyan boxes: set of 24 WVCs surrounding that red-framed, covering an area of $62.5 \times 62.5$ km². All acquisitions within these boxes and in the red-framed one are used to fit the linear trend of $\bar{\sigma}_{0,f}$. Noise regularization is only applied to the acquisitions in the red-framed WVC. Top (bottom) right: scatter plot of $\sigma_0$s vs. $f$ before (after) noise regularization is applied. Acquisitions are segregated according to the polarization of the signal (H-Pol or V-Pol) and the view (aft or fore). HH (VV) stands for H-Pol (V-Pol) and A (F) stands for aft (fore). (For interpretation of the references to color in this figure legend, the reader is referred to the web version of this article.)
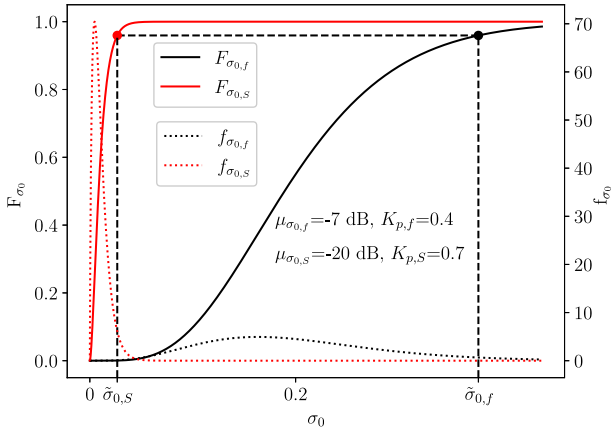


**Fig. 2.** Solid black (red) curve represents the CDF of the land-contaminated (sea) $\sigma_0$s, whose expected value is $-7$ dB ($-20$ dB) and $K_p$ is equal to 0.7 (0.4). The dotted black (red) curve represents the pdf of the land-contaminated (sea) $\sigma_0$s. Left (right) $y$-axis refers to CDFs (pdfs). $\tilde{\sigma}_{0,f}$ is a realization of land-contaminated $\sigma_0$s, whose corrected value is represented by $\tilde{\sigma}_{0,S}$. The case depicted here represents a typical scenario of a QuikSCAT inner beam coastal acquisition with an external slice (index 7 on a 0-based indexing) when the wind speed is around 10 ms$^{-1}$. (For interpretation of the references to color in this figure legend, the reader is referred to the web version of this article.)

threshold value was considered adequate to keep distortions negligible. A finer tuning of this value is beyond the scope of this paper.

$\bar{\sigma}_{0,f}$ and $\bar{\sigma}_{0,S}$ are also used to query the corresponding $K_p$s from a precomputed LUT of $K_p(\bar{\sigma}_0, slice, pol, view)$. The LUT of the precomputed $K_p$ is estimated from the former fourteen orbits listed in Table A.5, following the methodology described in Grieco et al. (2022b).

This procedure is employed to correct only the acquisitions dropping in the red-framed WVC.

Fig. 2 can help better understand how noise regularization works. It is based on simulated data, with realistic values, for the sake of

explaining how the algorithm works. In this figure, the black (red) solid curve represents the CDF of land-contaminated (sea) acquisitions, when their expected value is equal to $-7$ dB ($-20$ dB). Instead, the corresponding land-contaminated (sea) pdf is represented by the black (red) dotted curve. One random realization of land-contaminated acquisitions, indicated with the symbol $\tilde{\phantom{x}}$, is represented by $\tilde{\sigma}_{0,f}$, whose value is equal to $-4.2$ dB and its CDF value is marked with a black dot. This value is equal to the expected value plus two standard deviations, which is representative of a very noisy value. The corrected value is equal to $\tilde{\sigma}_{0,S}$ ($-15.7$ dB). Note that this case depicts a typical QuikSCAT acquisition with an external slice of the inner beam in a situation where the wind over sea is around 10 ms$^{-1}$. In this case, $K_{p,f}$ ($K_{p,S}$) is around 0.4 (0.7). External QuikSCAT slices are well known to be very noisy with respect to those central (Grieco et al., 2022b). Note that both pdfs are quite different from Gaussian distributions with the same expected values and standard deviations (not shown).

The analytical CDFs used in this method are positive definite, therefore cannot deal with negative contaminated $\sigma_0$s, unless LCR is lower than 2%, in which case they are not corrected. This occurs in 742 cases (0.03%) of the QCed negative $\sigma_0$s. This aspect will be improved but does not represent an important limit of the method, as shown in Section 3.2.

### 3.2. QuikSCAT wind retrieval scheme

The wind retrievals shown in this paper are obtained using PenWP (Verhoef et al., 2022). QuikSCAT slices are first allocated in WVCs with a grid spacing of 12.5 km and size of 17.5 km, following a "drop-in-the-bucket" procedure (Lindsley and Long, 2016); then they are averaged to obtain four different "views"; finally, a Multiple Solution Scheme (MSS) (Portabella and Stoffelen, 2004) is applied to retrieve the winds. A QC procedure is applied after the retrieval stage has been performed. All the details relating to the software and the references relating to the implemented methods can be found in Verhoef et al. (2022).
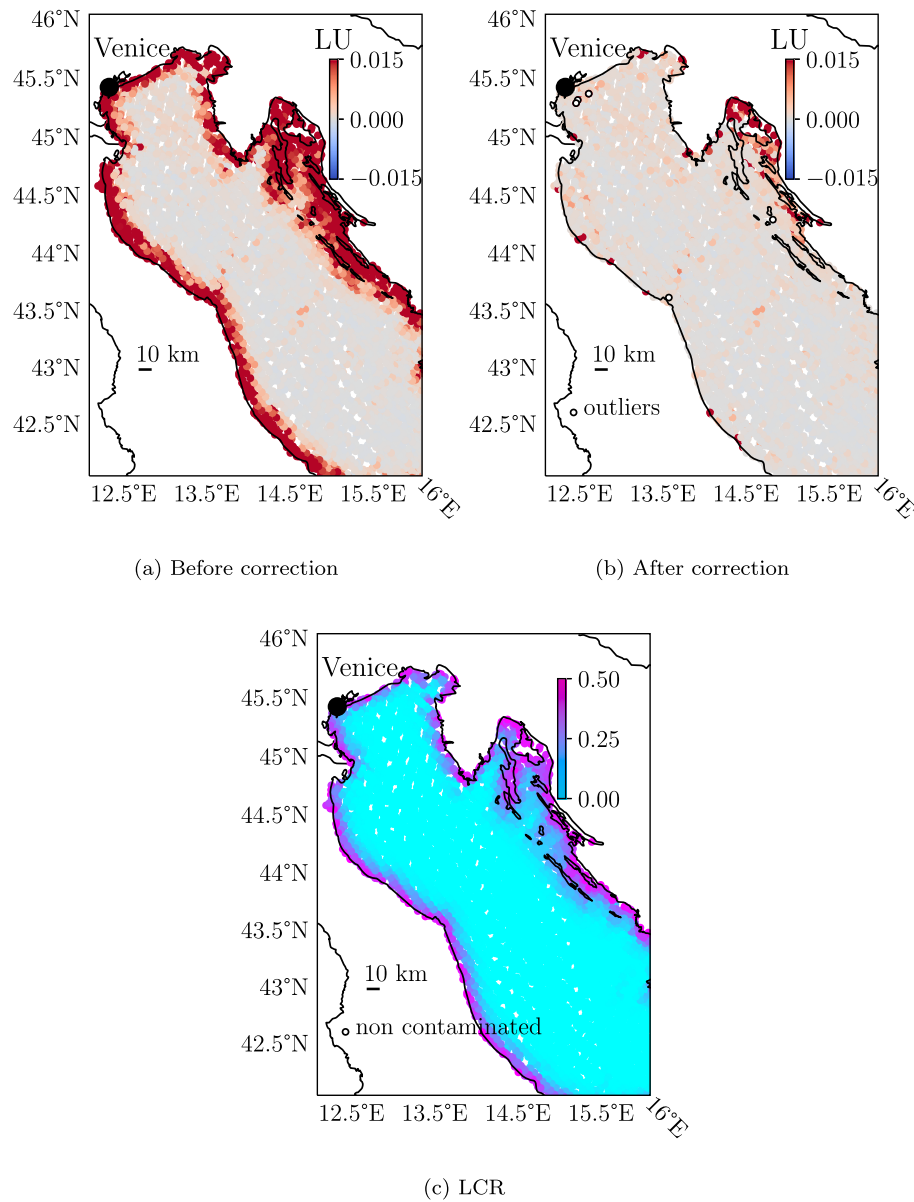
(a) Before correction

(b) After correction

(c) LCR

**Fig. 3.** Top left (right): $\sigma_0$ in linear units (LU) before (after) correction in the Adriatic basin, in the Mediterranean Sea. These images are extracted from the orbit with revolution ID equal to 40653. The small white spots on the sea are due to the sampling features of QuikSCAT. Empty circles (outliers) represent the slices for which noise regularization produces missing values. The position of the lagoon city of Venice is marked with a large black circle. Bottom: LCR in the same area. Non-contaminated acquisitions are marked with white black-framed circles (not visible because overlapped by those contaminated). (For interpretation of the references to color in this figure legend, the reader is referred to the web version of this article.)

### 3.3. ASAR wind retrieval scheme

The wind field from the ASAR image has been derived by a deep learning methodology based on a residual neural network (ResNet), which retrieves the wind direction then used to estimate the wind speed using the C_SARMOD2 GMF. The ResNet model had been trained using 27 ASAR WMS, listed in Table A.6, and the ECMWF operational forecast winds at 0.125° of model resolution (Zanchetto and Zecchetto, 2021). The 27 training images have been processed with the ESA Sentinel Application Platform (SNAP) in order to obtain calibrated images and the land–sea mask. SNAP can be downloaded for free from the following link: https://step.esa.int/main/toolboxes/snap/. The original SAR images at 75 m pixel have been undersampled to 300 m by the SNAP low pass filtering tool, to reduce the backscatter noise and filter out the gravity waves, if present. ResNet has been applied to Sentinel-1 images over the Venice Lagoon area (Zecchetto and Zanchetta, 2022), showing high reliability when compared with in-situ data. This method opened

the possibility to study the wind field variability close to coast, thanks to the high spatial grid (900 m) of the resulting wind fields, which show unprecedented details.

### 4. Results and discussion

Three different experiments have been set-up to prove the effectiveness of noise regularization on coastal wind retrievals. They are summarized in Table 3. All experiments are run over the entire dataset described in Section 2.1.

CTRL stands for "Control", and represents the state-of-the-art procedure of wind retrievals from QuikSCAT at the Ocean Sea Ice Satellite Application Facility of the European Agency for the Exploitation of Meteorological Satellites (EUMETSAT OSI SAF). For this experiment, the threshold value for LCR is set to 0.02. This means that all acquisitions with land contamination higher than 2% are discarded. NC stands for "Non Corrected". In this experiment, all acquisitions with
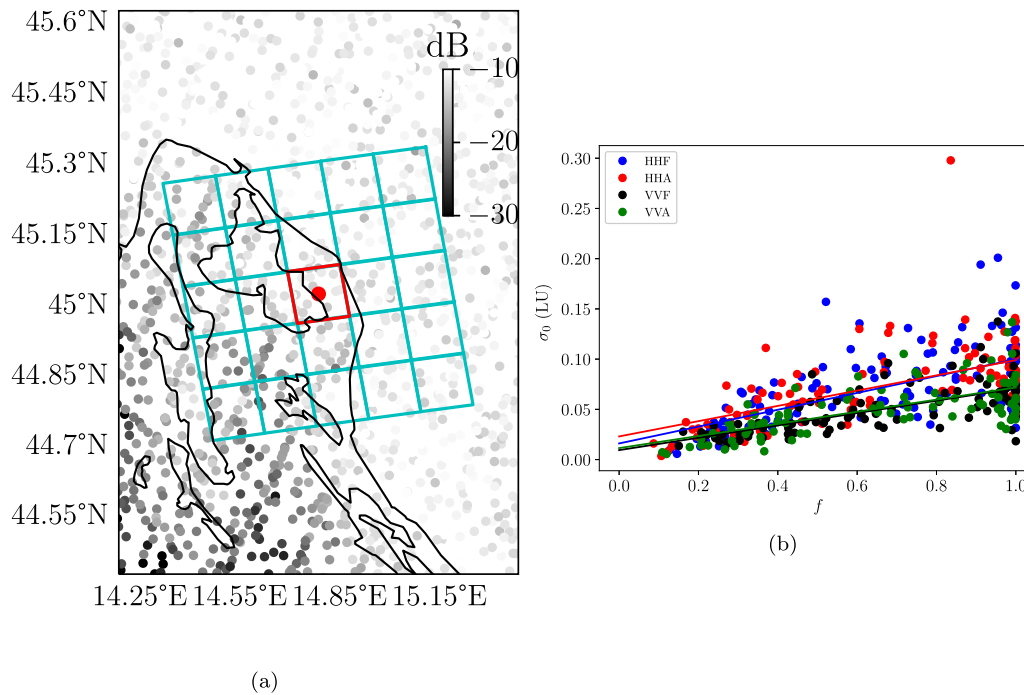
**Fig. 4.** Left: map of $\sigma_0$s in a coastal area offshore Croatia, in the Adriatic basin, in the Mediterranean Sea. Gray markers represent the slice centroids. Their colors represent the $\sigma_0$ values in logarithmic units (dB). Right: scatter plot of $\sigma_0$s dropping in the cyan-red matrix depicted on the left *vs.* $f$ in linear units (LU) segregated according to the four QuikSCAT flavors. HH (VV) stands for H-Pol (V-Pol) and A (F) stands for aft (fore). (For interpretation of the references to color in this figure legend, the reader is referred to the web version of this article.)

**Table 3**
Table of experiments. CTRL stands for "Control", NC for "Non Corrected" and NR for "Noise Regularization". All acquisitions with LCR ($f$) higher than $f$ th are discarded.

| Name | $f$ th | Noise regularization |
|------|--------|----------------------|
| CTRL | 0.02 | NO |
| NC | 0.5 | NO |
| NR | 0.5 | YES |

land contamination lower than 50% are used in the retrieval without applying any corrections. Finally, NR stands for "Noise Regularization". In this experiment, all acquisitions with land contamination higher than 50% are discarded and noise regularization is applied.

The comparison between NR and CTRL informs about the effectiveness of noise regularization in improving coastal sampling. The comparison between NR and NC informs about the effectiveness of noise regularization to reduce coastal wind biases due to land contamination.

The impact of noise regularization on $\sigma_0$ is shown in Section 4.1, based on a visual comparison between $\sigma_0$ before and after any corrections are applied, in the Adriatic basin, in the Mediterranean Sea. It is a narrow ($\approx$150 km of maximum width) semi-enclosed basin, where land contamination is present almost everywhere. The impact on the retrievals is shown in Section 4.2. Finally, in Section 4.3, the QuikSCAT-derived coastal winds are compared to the ASAR-derived winds in a coastal area offshore Norway.

### 4.1. Impacts of noise regularization on $\sigma_0$

Figs. 3(a) 3(b) shows the $\sigma_0$ map in linear units (LU) before (after) noise regularization is applied in the Adriatic basin, in the Mediterranean Sea. The colorbar is of the kind "coolwarm" to emphasize the presence of any negative values. Coastal contamination is highlighted by the intense red coastal band, whose width is around 15 km. After noise regularization is applied, coastal contamination disappears almost everywhere, except along the innermost Croatian islands of the Kvarner

gulf (north-eastern part of the basin), even if the contamination is dramatically reduced. This happens because, in such coastal areas, all the acquisitions in the $5 \times 5$ matrix used to fit $\bar{\sigma}_{0,f}$ are highly contaminated and the estimate of $\bar{\sigma}_{0,S}$ is not reliable. Fig. 4 shows one of these cases. Note that no acquisitions with land contamination less than 2% are present and the estimated $\bar{\sigma}_{0,S}$ for both H-Pol flavors are very high with respect to the surrounding sea areas ($\bar{\sigma}_{0,S}^{HHF} = -17.94$ dB and $\bar{\sigma}_{0,S}^{HHA} = -16.37$ dB). Furthermore, the MSEs of the four linear fits are much smaller than the corresponding median values, showing that even if the fit is good, the corrected biases can be severely biased if $\bar{\sigma}_{0,S}$ is biased. The incidence of such occurrences (indeed very limited) may be reduced by enlarging the size of the coastal area used to fit the $\bar{\sigma}_{0,f}$ curves, until an appropriate number of non-contaminated $\sigma_0$s is included in the fitting procedure, or, the correction procedure can be skipped and an appropriate flag is raised. However, an estimate of $\bar{\sigma}_{0,S}$ representative of an area farther than 80–100 km from the WVC of interest could not be representative of the target area, especially in zones characterized by the extensive presence of islands and mountains, such as the Kvarner gulf. This aspect will be further investigated in the upcoming future. This map, and others not shown for the sake of brevity, prove the effectiveness of noise regularization in reducing coastal contamination. The white black-framed circles in Fig. 3(b) represent the slices for which noise regularization produces missing values. This happens when $\sigma_0$ is negative. As already reported in Section 2, this concerns about 0.03% of all QCed negative $\sigma_0$ cases.

Note that coastal contamination impacts at distances much larger than what can be visually appreciated. To prove this, Fig. 3(c) shows the LCR map in the same basin. It is apparent that coastal contamination is present everywhere in narrow basins such as the Adriatic. Non-contaminated acquisitions are represented with white black-framed circles; however, they are not visible because they are overlapped by those contaminated. Note that, due to slice footprint asymmetry, land contamination depends on its orientation w.r.t. the coastline.

Finally, we have investigated the possibility that local $\sigma_0$ variability on land and sea can affect the linear fit and then the accuracy of the correction methodology. For this purpose, the excess of $\sigma_0$ variance
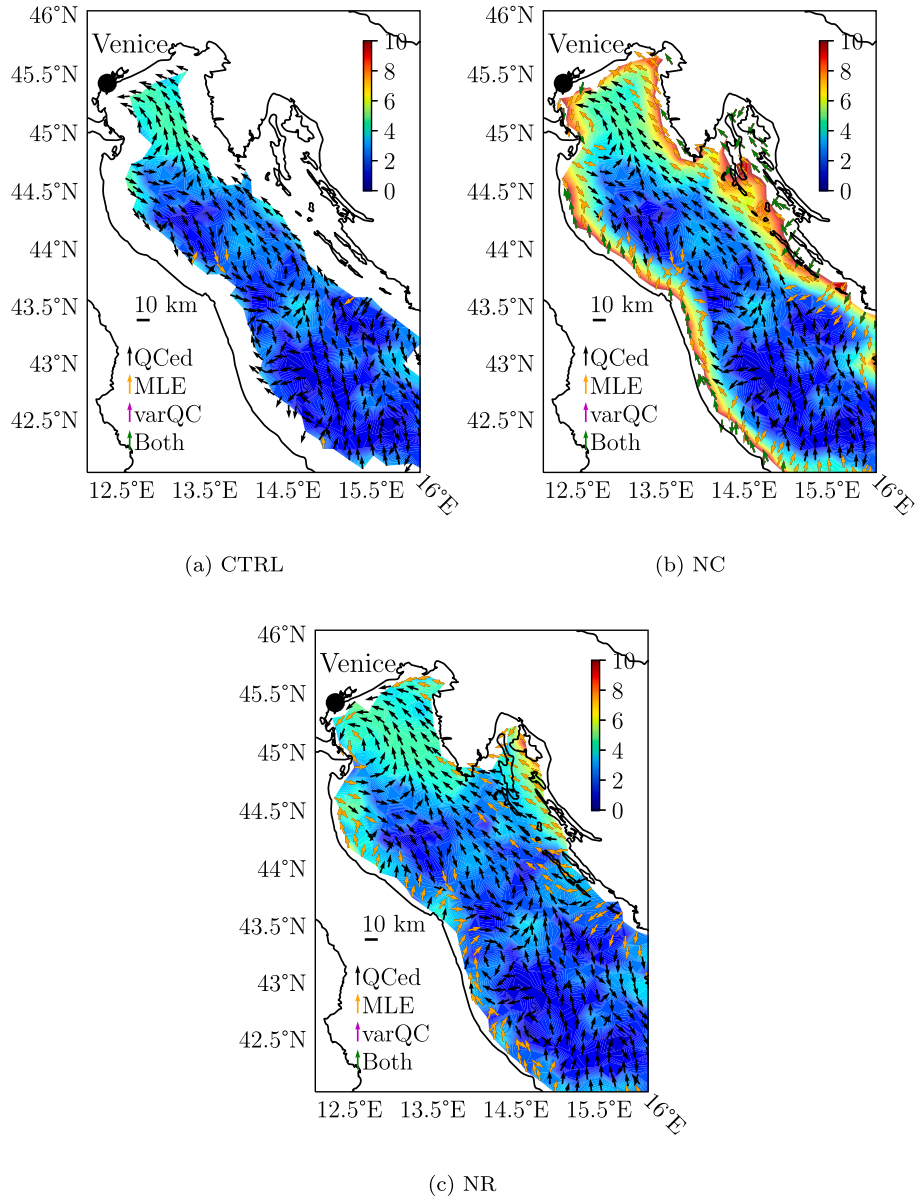
(a) CTRL

(b) NC

(c) NR

**Fig. 5.** Top left: wind field in the Adriatic basin (Mediterranean Sea) obtained with the CTRL experiment. The contour plot represents the wind speed in ms$^{-1}$. Arrows represent only the wind direction. "QCed" stands for Quality Controlled; "MLE" stands for Maximum Likelihood Estimator quality flag; "VarQC" stands for variational quality control flag; finally, "Both" stands that both MLE and VarQC flags are raised. Top right (bottom): same as top left but for the NC (NR) experiment. (For interpretation of the references to color in this figure legend, the reader is referred to the web version of this article.)

due to geophysical variability has been estimated with the following formula:

$$\bar{\epsilon}_g^2 = \bar{\epsilon}^2 - (K_p \bar{\sigma}_0)^2 \qquad (10)$$

We have verified that the correlation between $\sigma_e^2$ and $\bar{\epsilon}_g^2$ normalized by $\bar{\sigma}_0^2$ is negligible on sea, and very weak (at most around 0.35) on land. Furthermore, there is not any apparent correlation between $\bar{\epsilon}_g^2$ and the corrected $\sigma_0$s.

### 4.2. Impact of noise regularization on the retrieved winds

Fig. 5(a) shows the wind retrievals in the Adriatic basin for the CTRL experiment. The contour fill map represents the wind speed, while the arrows represent the wind direction. Black arrows represent winds that pass the a-posteriori QC tests on the retrievals; yellow arrows represent those for which the Maximum Likelihood Estimator (MLE) flag is raised; magenta arrows represent those for which the so-called VarQC flag

is raised; finally, green arrows represent the instances for which both MLE and VarQC flags are raised. The MLE residual test fails when the deviation of the NRCS measurements from the GMF exceeds a given threshold value, while the VarQC test fails in case of inconsistency in the 2-D variational ambiguity removal (2-DVAR) procedure (Xu and Stoffelen, 2020; Portabella et al., 2012). It is apparent that the coastal band within 20–30 km from the coastline is not sampled. Fig. 5(b) shows the same map but for the NC experiment. Here, the coastal band is much more sampled, but the retrieved winds are apparently biased. Finally, Fig. 5(c) shows the same map when noise regularization is applied (NR experiment). Now, the coastal band is properly sampled up to few kilometers to the coast and the coastal wind biases are dramatically reduced, except in the innermost part of the Kvarner gulf, as expected. The cyclonic structure in the north-western part of the basin that can only be guessed in the CTRL experiment, is much better sampled in NR. In particular, the light green pattern centered at around 45°N–13°E, characterized by the presence of sirocco is now better sampled towards the coast, without signs of any coastal gradients due
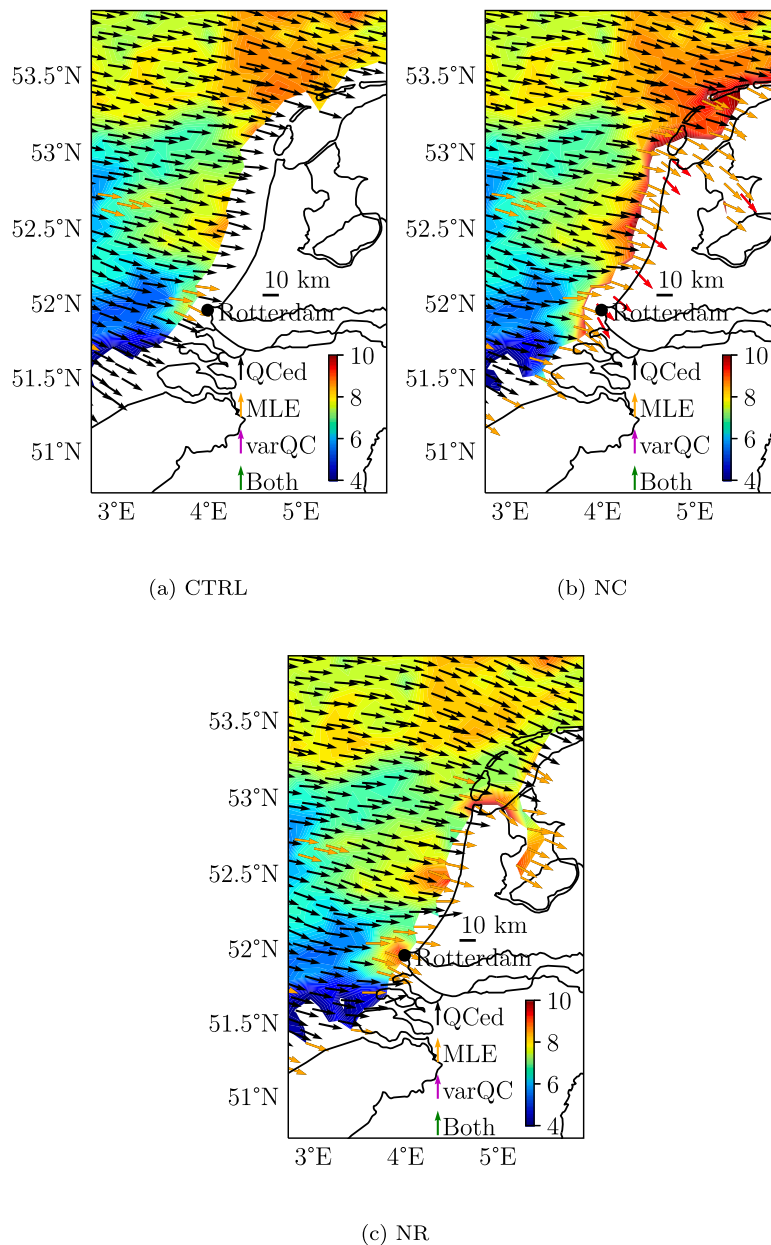
**Fig. 6.** Top left: wind field offshore the Netherlands obtained with the CTRL experiment. The contour plot represents the wind speed in ms⁻¹. Arrows represent only the wind direction. "QCed" stands for Quality Controlled; "MLE" stands for Maximum Likelihood Estimator quality flag; "VarQC" stands for variational quality control flag; finally, "Both" stands that both MLE and VarQC flags are raised. Top right (bottom): same as top left but for the NC (NR) experiment.

to residual coastal contamination. On the other side, the light-green pattern centered at around 44.5°N–12.5°E, characterized by northwestern winds is much better sampled in the NR experiment, while it could only be guessed in the CTRL experiment.

Accurate scatterometer-derived coastal winds are expected to further improve high-resolution ocean wind forcing products such as the scatterometer-blended ECMWF Reanalysis ERA* (Trindade et al., 2020; Trindade, 2023) or the scatterometer-tuned ECMWF winds in the Adriatic sea presented in the context of the ESA project E-Surge by Zecchetto et al. (2015) along the coasts.

The number of MLE-flagged WVCs is not negligible along the coasts. However, both wind speed and direction seem to be consistent with the surrounding QCed WVCs in most of these cases. This suggests that MLE should probably be better tuned in coastal areas. This aspect goes beyond the scope of this paper and is left for future studies.

Fig. 6 shows the wind retrievals offshore the Netherlands. Also in this case, the improvement in both sampling and accuracy is apparent

when noise regularization is applied. In particular, note that good QCed WVCs are also present in the internal sea named IJsselmeer, in the north-eastern part of the map. Note also the high-wind-speed spot centered around the Rotterdam harbor. This is likely due to residual contamination by ships, due to intense traffic in the most active European harbor. More in general, large coastal $\sigma_0$ heterogeneities need further attention.

Fig. 7 shows the ratio of the QCed WVCs sampled in the NR experiment w.r.t. CTRL, as a function of distance from the coastline, expressed in %. "os" stands for "offshore". The blue, green and red dash-dotted lines represent the cumulative ratios in the first 10, 20 and 30 km from the coastline. It is apparent that the sampling ratio dramatically improves in the first 10 km to the coast, with a peak of more than 450% within 5 km. This high figure is not surprising because the occurrences of QCed WVCs in CTRL are expected to be close to 0. In fact, this happens in special coastal areas characterized by the presence of very small islands, for which LCR is lower than
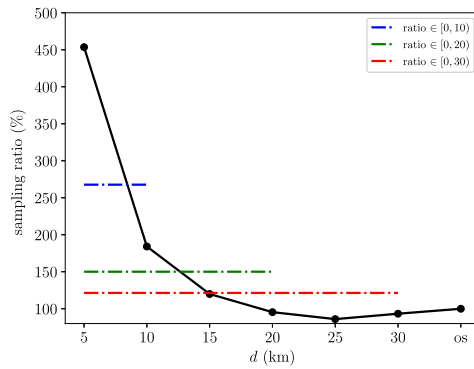
**Fig. 7.** Sampling ratio variation (%) of QCed WVCs obtained with the NR experiment w.r.t. CTRL as a function of the distance from the coastline. "os" stands for offshore. Blue, green and red dash-dotted lines represent the cumulative sampling variation in the first 10, 20 and 30 km to the coast, respectively. (For interpretation of the references to color in this figure legend, the reader is referred to the web version of this article.)

2% and good retrievals are possible. An example of such areas is represented by the Dahlak archipelago, in the Red Sea (not shown for the sake of brevity). Instead, NR sampling within 5 km from the coast happens almost everywhere offshore continental coastlines, as shown in Figs. 5 and 6. Note also that these sampling figures could underestimate the real sampling improvement, since lots of MLE-flagged WVCs are expected to be false positive, as discussed previously. Finally, note that the sampling ratio goes below 1 when the distance from the coastline is higher than 20 km. This may seem counterintuitive or could lead to the conclusion that it is degraded. Instead, this is due to the optimization of the WVC grid after retrieval is performed. In fact, it has been demonstrated (not shown here) that WVC centroids are on average further from the coast in CTRL w.r.t. NR, due to the massive discard in the former land-contaminated $\sigma_0$s (Grieco et al., 2022a).

### 4.3. Comparison with SAR-derived winds

Fig. 8(a) shows the map of $\sigma_0$ in logarithmic units (dB) acquired by the Envisat ASAR VV channel on the 24th of November 2008 at 8:16 P.M. UTC, from which the wind field at 900 m of grid spacing has been retrieved using the ResNet methodology described in Section 3.3.

Blue arrows in Fig. 8(b) represent the QuikSCAT-derived wind field extracted from the orbit with revolution ID equal to 49132, after noise regularization is applied, at 8:01 P.M. UTC of the 24th of November 2008, 15 min before the ASAR pass. Red arrows represent the collocated ASAR-derived winds averaged over a circular area of 15 km centered around the QuikSCAT WVC centroids. The two vector winds are expected to have a similar spatial resolution. Table 4 reports the statistics of the comparison between scatterometer and SAR-derived winds, segregated according to the distance to the coastline. $U$ stands for wind speed, $\phi$ for wind direction, RMS for root mean square difference and vRMS for vector RMS. The number of available pairs is reported in the last column. It is apparent that the comparison worsens when approaching the coast, perhaps due to errors in the land correction procedure, but may be also due to other causes, such as enhanced coastal variability and/or model understimation (Cavaleri et al., 2024). The vRMS is higher than the figures indicated in Vogelzang and Stoffelen (2022b), demonstrating that ResNet-derived winds are still rather noisy.

### 5. Conclusions and future work

This study presents the implementation of a correction scheme applied to the coastal Normalized Radar Cross Sections ($\sigma_0$s) acquired by the SeaWinds scatterometer with the aim of mitigating land contamination. This is an analytical scheme requiring that the corrected values

**Table 4**

Statistics of the comparison between scatterometer and SAR-derived winds. $U$ stands for wind speed, $\phi$ for wind direction, RMS for root mean square difference and vRMS for vector RMS. Data are segregated according to the distance to the coastline, as reported in the first column. The number of available scatterometer-SAR pairs is reported in the last column.

| d (km) | bias($U$) (ms$^{-1}$) | RMS($U$) (ms$^{-1}$) | bias($\phi$) (°) | RMS($\phi$) (°) | vRMS (ms$^{-1}$) | # of pairs |
|---|---|---|---|---|---|---|
| 40 | −0.3 | 1.4 | 10 | 23 | 3.0 | 262 |
| 80 | −0.1 | 1.2 | 7 | 21 | 2.8 | 409 |
| All | −0.1 | 1.1 | 0 | 18 | 2.8 | 1008 |

**Table A.5**

List of QuikSCAT FR files used in this study. All QuikSCAT FR files are provided in hdf4 format.

| QuikSCAT Full Resolution file names |
|---|
| QS_S1B40651.20071011559 |
| QS_S1B40652.20071011600 |
| QS_S1B40653.20071011631 |
| QS_S1B40654.20071011604 |
| QS_S1B40655.20071011605 |
| QS_S1B40656.20071011606 |
| QS_S1B40657.20071011607 |
| QS_S1B40658.20071011608 |
| QS_S1B40659.20071011608 |
| QS_S1B40660.20071011608 |
| QS_S1B40661.20071011608 |
| QS_S1B40662.20071011612 |
| QS_S1B40663.20071011612 |
| QS_S1B40664.20071011612 |
| QS_S1B49132.20083300135 |

comply with the expected cumulative distribution functions (CDF). The analytical models of the contaminated and non-contaminated CDFs rely on the estimation of the specific levels of noise and the expected values of contaminated and non-contaminated $\sigma_0$s.

The scheme is applied to a set of fifteen QuikSCAT orbits and its effectiveness is proven on the semi-enclosed Adriatic basin, in the Mediterranean Sea, showing a dramatic mitigation of land contamination. The applicability of this method is limited by the presence of numerous small-to-medium sized islands, where land contamination may persist after its application. In addition, it cannot deal with negative $\sigma_0$s with contamination levels exceeding 2%. Actually, this does not represent a big issue, since their occurrence is limited to 0.03% of all negative good quality $\sigma_0$s. However, this aspect will be addressed in the upcoming future. Furthermore, the eventual presence of residual contamination will be assessed, and the analytical model will be updated if necessary.

The results of three retrieval exercises are presented in three area tests, with the aim of assessing the capability of this method to improve coastal sampling and wind retrieval accuracy along the coasts. Coastal sampling dramatically improves w.r.t. the state-of-the art procedure implemented at EUMETSAT OSI SAF, with a peak of 300% within 10 km to the coastline. However, this figure could underestimate the real potential of this technique because lots of flagged winds are consistent with the surrounding good quality winds; a better tuning of the a-posteriori MLE test is expected to increase the number of good retrievals. This aspect is also left for the future.

Finally, QuikSCAT-derived winds are compared with Envisat ASAR-derived winds in a coastal area offshore Norway. Wind patterns from ASAR and QuikSCAT are in very good agreement, demonstrating that SAR-derived winds can be used to validate coastal scatterometer-derived winds and that scatterometer-derived winds can be used to validate SAR-derived winds in open ocean. However, an extensive validation of QuikSCAT-derived winds is necessary, and will be carried out with a much larger dataset.

SARs, similarly to scatterometers, measure instantaneous winds over a given area (even if with different coverages and resolutions). Unlike
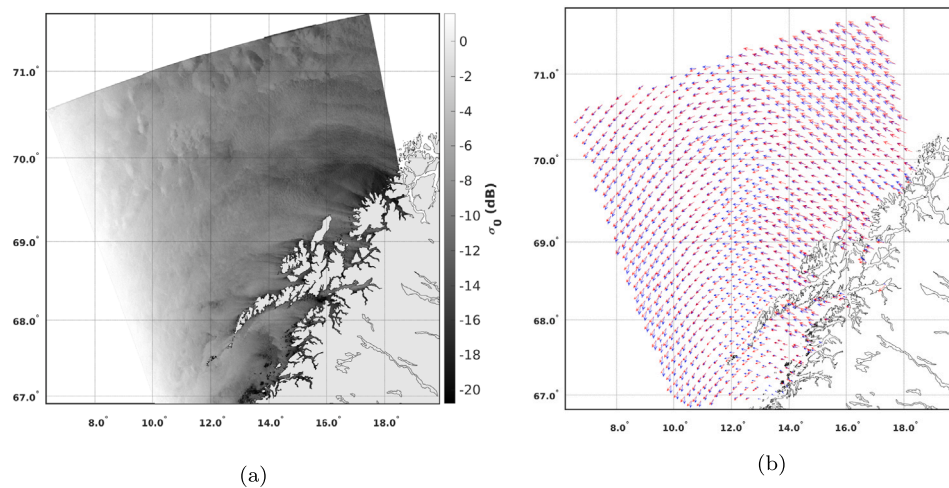
**Fig. 8.** Left: $\sigma_0$ in logarithmic units (dB) acquired by the ASAR VV channel onboard Envisat on the 24th of November 2008 at 8:16 P.M. UTC. Right: blue arrows represent the QuikSCAT-derived winds; red arrows represent the ASAR-derived winds averaged on a circle with a 15 km radius centered around the QuikSCAT 12.5 km WVC centroids; black markers represent the rainy WVCs. Finally, the statistics relating to the vector RMS error (vRMS) of the two wind fields and the RMS in direction (DirDiff) are reported in the panel. (For interpretation of the references to color in this figure legend, the reader is referred to the web version of this article.)

**Table A.6**
First 27 lines: list of the ASAR WSM files used to train the ResNet model to retrieve wind direction. Last line: filename of the ASAR image used to validate QuikSCAT-derived winds offshore Norway.

| ASAR file names |
| --- |
| ASA_WSM_1PNDSI20060102_105652_000001352043_00495_20088_0000.N1 |
| ASA_WSM_1PNDSI20060105_110206_000001352044_00037_20131_0000.N1 |
| ASA_WSM_1PNDSI20060209_110128_000001352045_00037_20632_0000.N1 |
| ASA_WSM_1PNDSI20060423_110746_000001352047_00080_21677_0000.N1 |
| ASA_WSM_1PNDSI20080424_110058_000000982068_00037_32155_0000.N1 |
| ASA_WSM_1PNDSI20090225_230348_000001532076_00431_36557_0000.N1 |
| ASA_WSM_1PNDSI20101207_104933_000003063097_00152_45856_0000.N1 |
| ASA_WSM_1PNDSI20101215_110049_000002943097_00267_45971_0000.N1 |
| ASA_WSM_1PNDSI20101220_111651_000002513097_00339_46043_0000.N1 |
| ASA_WSM_1PNDSI20110214_231522_000000923099_00289_46855_0000.N1 |
| ASA_WSM_1PNDSI20110604_224500_000000923103_00145_48435_0000.N1 |
| ASA_WSM_1PNDSI20101218_105048_000002883097_00310_46014_0000.N1 |
| ASA_WSM_1PNDSI20080309_194917_000000922066_00386_31502_0000.N1 |
| ASA_WSM_1PNDSI20081212_190830_000005142074_00357_35481_0000.N1 |
| ASA_WSM_1PNDSI20080427_190624_000003732068_00085_32203_0000.N1 |
| ASA_WSM_1PNDSI20080115_212117_000002942065_00115_30730_0000.N1 |
| ASA_WSM_1PNDSI20080525_210650_000000922068_00487_32605_0000.N1 |
| ASA_WSM_1PNDSI20080209_200033_000000922065_00472_31087_0000.N1 |
| ASA_WSM_1PNDSI20080816_192054_000001222071_00171_33792_0000.N1 |
| ASA_WSM_1PNDSI20081118_101825_000001532074_00008_35132_0000.N1 |
| ASA_WSM_1PNDSI20081217_195335_000001842074_00429_35553_0000.N1 |
| ASA_WSM_1PNDSI20080923_210228_000002142072_00215_34337_0000.N1 |
| ASA_WSM_1PNDSI20080103_205958_000001902064_00444_30558_0000.N1 |
| ASA_WSM_1PNDSI20080206_100410_000001842065_00423_31038_0000.N1 |
| ASA_WSM_1PNDSI20080920_191817_000002392072_00171_34293_0000.N1 |
| ASA_WSM_1PNDSI20080912_102043_000002202072_00051_34173_0000.N1 |
| ASA_WSM_1PNDSI20080808_102047_000001902071_00051_33672_0000.N1 |
| ASA_WSM_1PNDSI20081124_201719_000000922074_00100_35224_0000.N1 |

NWP models, SAR-derived winds are sensitive to local orography and have a much higher spatial resolution; therefore, they are expected to be very useful for the validation of scatterometer-derived winds. SAR is expected to be used more and more as a diagnostic and validation tool for coastal winds in the upcoming future. Buoys measure winds on a given point over a time interval of several minutes. Their use for wind validation is very appropriate in the open ocean, but may be problematic in coastal areas. However, a quadruple collocation analysis among scatterometers, SARs, NWPs and buoys is expected to be beneficial in validating scatterometer-derived winds and assessing the limits of this approach in coastal areas. More in details, when comparing buoys with scatterometer, ECMWF model and SAR, there are several objectives that can be pursued: (a) Verify land correction; this

is, within 25 km from the coast winds may deteriorate due to poor land correction; (b) Verify SAR winds; in particular, SAR has high spatial resolution, but poor geophysical resolution; (c) Verify model winds; e.g., ECMWF model winds deteriorate within 25 km towards the coast (probably due to numerical diffusion); (d) Verify representativeness errors of the buoys; this is, as the buoys get closed to complex land–sea boundaries, wind variability tends to increase. An extensive analysis of this kind is planned for the future.

Noise regularization will be also compared with other state-of-the-art mitigation schemes, such as that applied to produce the NASA JPL QuikSCAT product v4.1. Finally, this methodology will be applied to all pencil-beam scatterometers, such as those of the Chinese Hayang-2 family and the Indian ScatSat-1 and OceanSat 2 and 3.

### CRediT authorship contribution statement

**Giuseppe Grieco:** Writing – review & editing, Writing – original draft, Visualization, Validation, Software, Methodology, Investigation, Funding acquisition, Formal analysis, Data curation, Conceptualization. **Marcos Portabella:** Writing – review & editing, Supervision, Funding acquisition, Conceptualization. **Ad Stoffelen:** Writing – review & editing, Supervision, Funding acquisition, Conceptualization. **Anton Verhoef:** Writing – review & editing, Supervision, Software. **Jur Vogelzang:** Writing – review & editing, Supervision, Software, Conceptualization. **Andrea Zanchetta:** Validation, Software, Methodology, Data curation. **Stefano Zecchetto:** Writing – review & editing, Visualization, Validation, Methodology, Data curation.

### Declaration of competing interest

The authors declare that they have no known competing financial interests or personal relationships that could have appeared to influence the work reported in this paper.

### Data availability

Data will be made available on request.

## Acknowledgments

## Appendix A

The full list of QuikSCAT and ASAR files used in this study are reported in Tables A.5 and A.6, respectively, for the sake of repeatability.

## References

Anderson, C., Bonekamp, H., Duff, C., Figa-Saldana, J., Wilson, J.J.W., 2012. Analysis of ASCAT ocean backscatter measurement noise. IEEE Trans. Geosci. Remote Sens. 50, 2449–2457. http://dx.doi.org/10.1109/TGRS.2012.2190739.

Bourassa, M.A., Meissner, T., Cerovecki, I., Chang, P.S., Dong, X., De Chiara, G., Donlon, C., Dukhovskoy, D.S., Elya, J., Fore, A., Fewings, M.R., Foster, R.C., Gille, S.T., Haus, B.K., Hristova-Veleva, S., Holbach, H.M., Jelenak, Z., Knaff, J.A., Kranz, S.A., Manaster, A., Mazloff, M., Mears, C., Mouche, A., Portabella, M., Reul, N., Ricciardulli, L., Rodriguez, E., Sampson, C., Solis, D., Stoffelen, A., Stukel, M.R., Stiles, B., Weissman, D., Wentz, F., 2019. Remotely sensed winds and wind stresses for marine forecasting and ocean modeling. Front. Mar. Sci. 6, http://dx.doi.org/10.3389/fmars.2019.00443, URL: https://www.frontiersin.org/articles/10.3389/fmars.2019.00443/full.

Cavaleri, L., Balsamo, G., Beljaars, A., Bertotti, L., Davison, S., Edwards, J., Kanehama, T., Wedi, N., 2024. ECMWF and UK met office offshore blowing winds: Impact of horizontal resolution and coastal orography. J. Geophys. Res.: Atmos. 129, http://dx.doi.org/10.1029/2023JD039673, URL: https://agupubs.onlinelibrary.wiley.com/doi/abs/10.1029/2023JD039673, arXiv:https://agupubs.onlinelibrary.wiley.com/doi/pdf/10.1029/2023JD039673. e2023JD039673 2023JD039673.

Early, D.S., Long, D.G., 2001. Image reconstruction and enhanced resolution imaging from irregular samples. IEEE Trans. Geosci. Remote Sens. 39, 291–302. http://dx.doi.org/10.1109/36.905237.

Fore, A.G., Stiles, B.W., Strub, P.T., West, R.D., 2022. QuikSCAT climatological data record: Land contamination flagging and correction. Remote Sens. 14, http://dx.doi.org/10.3390/rs14102487, URL: https://www.mdpi.com/2072-4292/14/10/2487.

Grieco, G., Portabella, M., Vogelzang, J., Verhoef, A., Stoffelen, A., 2022a. Set-Up of PenWP for SeaWinds-Derived Coastal Winds. Technical Report, Istituto di Scienze Marine (ISMAR-CNR), OSI-SAF VS Technical Report # OSI-SAF 22-02.

Grieco, G., Stoffelen, A., Verhoef, A., Vogelzang, J., Portabella, M., 2022b. Analysis of data-derived SeaWinds normalized radar cross-section noise. Remote Sens. 14, URL: https://www.mdpi.com/2072-4292/14/21/5444.

Grieco, G., Stoffelen, A., Verhoef, A., Vogelzang, J., Portabella, M., 2022c. Correction of SeaWinds normalized radar cross sections for improved coastal winds. In: 2022 IEEE International Workshop on Metrology for the Sea; Learning to Measure Sea Health Parameters. MetroSea, pp. 383–387. http://dx.doi.org/10.1109/MetroSea55331.2022.9950798.

Lindsley, R.D., Long, D.G., 2016. Enhanced-resolution reconstruction of ASCAT backscatter measurements. IEEE Trans. Geosci. Remote Sens. 54, 2589–2601. http://dx.doi.org/10.1109/TGRS.2015.2503762.

Lungu, T., Callahan, P.S., 2006. QuikSCAT Science Data Product. User's Manual, 3.0 ed. JPL NASA, URL: https://archive.podaac.earthdata.nasa.gov/podaac-ops-cumulus-docs/quikscat/open/L1B/v2/docs/QSUG_v3.pdf.

Owen, M.P., Long, D.G., 2009. Land-contamination compensation for quikSCAT near-coastal wind retrieval. IEEE Trans. Geosci. Remote Sens. 47, 839–850.

Portabella, M., Stoffelen, A., 2004. A probabilistic approach for SeaWinds data assimilation. Q. J. R. Meteorol. Soc. 130, 127–152. http://dx.doi.org/10.1256/qj.02.205, URL: https://rmets.onlinelibrary.wiley.com/doi/abs/10.1256/qj.02.205, arXiv:https://rmets.onlinelibrary.wiley.com/doi/pdf/10.1256/qj.02.205.

Portabella, M., Stoffelen, A., Verhoef, A., Verspeek, J., 2012. A new method for improving scatterometer wind quality control. IEEE Geosci. Remote Sens. Lett. 9, 579–583. http://dx.doi.org/10.1109/LGRS.2011.2175435.

SeaPAC, 2006. Seawinds on quikSCAT level 1B time-ordered Earth-located sigma0 version 2. http://dx.doi.org/10.5067/QSXXX-L1B02, URL: http://podaac.jpl.nasa.gov/dataset/QSCAT_LEVEL_1B_V2.

Soisuvarn, S., Jelenak, Z., Chang, P.S., Zhu, Q., Shoup, C.G., 2023. High-Resolution Coastal winds from the NOAA near real-time ASCAT processor. IEEE Trans. Geosci. Remote Sens. 61, 1–12. http://dx.doi.org/10.1109/TGRS.2023.3279764.

Spencer, M.W., Wu, C., Long, D.G., 2000. Improved resolution backscatter measurements with the SeaWinds pencil-beam scatterometer. IEEE Trans. Geosci. Remote Sens. 38, 89–104.

Trindade, A., 2023. Development of high-resolution L4 ocean wind products. URL: http://hdl.handle.net/10803/687576.

Trindade, A., Portabella, M., Stoffelen, A., Lin, W., Verhoef, A., 2020. ERAstar: A high-resolution ocean forcing product. IEEE Trans. Geosci. Remote Sens. 58, 1337–1347. http://dx.doi.org/10.1109/TGRS.2019.2946019.

Vanhoff, et al., 2013. QuikSCAT level 3 near-coast wind and stress fields with Enhanced Coastal coverage (OSU): US West Coast Region.

Verhoef, A., Vogelzang, J., Verspeerk, J., Stoffelen, A., 2022. PenWP User Guide, 4.0.01 ed. NWP-SAF, URL: https://nwp-saf.eumetsat.int/site/download/documentation/scatterometer/penwp/NWPSAF-KN-UD-009_PenWP_User_Guide_v4.0.pdf.

Vogelzang, J., Stoffelen, A., 2022a. ASCAT Land Correction, Report for the EUMETSAT Ocean and Sea Ice SAF. Technical Report, Koninklijk Nederlands Meteorologisch Instituut, SAF/OSI/CDOP3/KNMI/TEC/TN/384.

Vogelzang, J., Stoffelen, A., 2022b. On the accuracy and consistency of quintuple collocation analysis of in situ, scatterometer, and NWP winds. Remote Sens. 14, http://dx.doi.org/10.3390/rs14184552, URL: https://www.mdpi.com/2072-4292/14/18/4552.

Xu, X., Stoffelen, A., 2020. Improved rain screening for Ku-band wind scatterometry. IEEE Trans. Geosci. Remote Sens. 58, 2494–2503. http://dx.doi.org/10.1109/TGRS.2019.2951726.

Zanchetta, A., Zecchetto, S., 2021. Wind direction retrieval from sentinel-1 SAR images using ResNet. Remote Sens. Environ. 253, 112178. http://dx.doi.org/10.1016/j.rse.2020.112178, URL: https://www.sciencedirect.com/science/article/pii/S0034425720305514.

Zecchetto, S., della Valle, A., De Biasio, F., 2015. Mitigation of ECMWF–scatterometer wind biases in view of storm surge applications in the Adriatic sea. Adv. Space Res. 55, 1291–1299. http://dx.doi.org/10.1016/j.asr.2014.12.011, URL: https://www.sciencedirect.com/science/article/pii/S0273117714007704.

Zecchetto, S., Zanchetta, A., 2022. Structure of high-resolution SAR winds over the Venice Lagoon Area. IEEE Trans. Geosci. Remote Sens. 60, 1–9. http://dx.doi.org/10.1109/TGRS.2022.3170705.